Analytica Chimica Acta 1229 (2022) 340383

Contents lists available at ScienceDirect

Analytica Chimica Acta

journal homepage: www.elsevier.com/locate/aca

Dual-mode colorimetric-photothermal sensing platform of acetylcholinesterase activity based on the peroxidase-like activity of Fe–N–C nanozyme

Liling Lu, Xuehan Hu, Ruijin Zeng, Qianyun Lin, Xue Huang, Meijin Li **, Dianping Tang *

Key Laboratory for Analytical Science of Food Safety and Biology (MOE & Fujian Province), Department of Chemistry, Fuzhou University, Fuzhou, 350108, People's Republic of China

HIGHLIGHTS

- A photothermal and colorimetric dual-readout sensor was constructed for acetylcholinesterase analysis.
- The Fe–N–C with excellent peroxidase-like activity was simply synthesized by hydrothermal method.
- A portable near-infrared imaging camera on a smartphone was used as readout.
- The proposed strategy can be used for the detection of acetylcholinesterase in human serum samples.

GRAPHICAL ABSTRACT

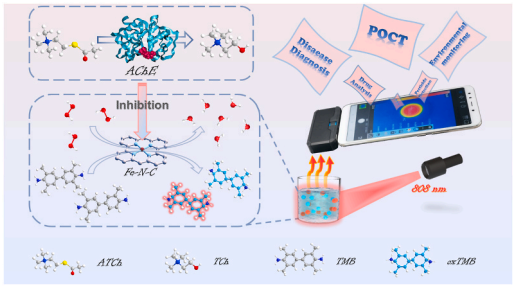

ARTICLE INFO

Keywords:
Photothermal
Dual-mode detection
Fe–N–C nanozyme
Peroxidase mimic
Acetylcholinesterase

ABSTRACT

Sensors based on colorimetry, fluorescence, and electrochemistry have been widely employed to detect acetylcholinesterase and its inhibitors, however, there are only a minority of strategies for AChE detection based on photothermal method. This work reports a versatile dual-mode colorimetric and photothermal biosensing platform for acetylcholinesterase (AChE) detection and its inhibitor (paraoxon-ethyl, a model of AChE inhibitors) monitor based on Fe–N–C/H_2O_2/3,3′,5,5′-tetramethylbenzidine (TMB) system. The Fe–N–C with abundant active Fe-Nx sites shows outstanding peroxidase-mimicking activity and can be used to promote the generation of •OH by H_2O_2 to oxidize TMB. However, the introduction of mercapto molecules tending to coordinate with metal atoms result in the block of action site in Fe–N–C, thereby decrease its peroxidase-mimetic activity. The designed biosensor principle is based on the block of active sites of Fe–N–C by thiocholine (TCh, one kind of mercapto molecules) that can be produced by acetylthiocholine (ATCh) in the presence of AChE. Under optimum conditions, the limit of detection (LOD) for AChE activity is 1.9 mU mL^{-1} (colorimetric) and 2.2 mU mL^{-1} (photothermal), while for paraoxon-ethyl is 0.012 μg mL^{-1} (colorimetric) and 0.013 μg mL^{-1} (photothermal), respectively. The assay we proposed not only can be designed to monitor AChE detection and its inhibitors, but also can be easily extended for the detection of other biomolecules relate to the generation or consumption of H_2O_2.

* Corresponding author.
** Corresponding author.
E-mail addresses: mjli@fzu.edu.cn (M. Li), dianping.tang@fzu.edu.cn (D. Tang).

https://doi.org/10.1016/j.aca.2022.340383
Received 16 August 2022; Accepted 8 September 2022
Available online 12 September 2022

1. Introduction

Acetylcholinesterase (AChE), one of the serine hydrolases principally existing in central nervous system, is capable to convert its natural substrate acetylcholine (ATCh) into acetate and choline rapidly, contributing to regulate the levels of ATCh and terminate neurotransmission [1–4]. It plays an extremely important part in biological signal transmission. Accumulating evidence has revealed that irregular expression of AChE is closely associated with neurodegenerative diseases, including Alzheimer's disease, Parkinson's disease, amyotrophic lateral sclerosis and Huntington's disease, development of drug-resistant bacterial strains and other adverse reactions [5–9]. Inhibiting the activity of AChE which would result in the aggregation of acetylcholine in synaptic transmission has been confirmed to be one of the effective strategies for neurodegenerative disease treatment [10]. In view of the adverse effect of the inhibitors of AChE abuse on the health and the environment, an efficient detection for AChE activity with high accuracy and convenient operation is of critical significance in biomedical diagnosis, environmental monitoring and so on. So far, a variety of high-sensitivity detection methods have been established and applied to detect AChE activity and corresponding inhibitors, including enzyme-linked immunosorbent assay [11], electrochemical method [12,13], mass spectrometry [14], *etc.* However, there are still some non-negligible weaknesses preventing these methods from on-site monitoring, such as false-positive or false-negative effects, time-consumption, and the demand of expensive instrumentation. Compared with these detection methods, colorimetric and photothermal methods are fast, economical, simple, and do not require an operation on expensive equipment [15–19]. These characteristics make colorimetric and photothermal methods stable for on-site AChE and Ops (organophosphorus pesticides) detection.

Colorimetric relies on color reactions that produce colored complexes and is one of the common strategies for monitoring various molecules. Colorimetric analysis requires color reactions with excellent selectivity and sensitivity, as well as constant product stability [20–22]. Up to now, enzymatic colorimetry is one of the most commonly used colorimetric methods, especially for nanozymes [23]. Liang et al. synthesized GeO_2 nanozymes for colorimetric sensing of AChE and Ops [24]. Coincidentally, Xiong et al. synthesized CeO_2 nanozymes for the sensitive detection of hydrogen peroxide and so on [25]. Unfortunately, these analytical assays depending on a single output of absorbance have certain limitations (the need microplate readers) in resource-poor settings. Hence, there remains a challenge of developing an assay with a low-cost readout and high portability to realize the point-of-care in resource-poor settings. The photothermal assay is based on the photothermal effect of photothermal materials, which mainly absorbs incident light and releases it in the form of thermal energy [26–28]. The key issue to photothermal analysis is to choose effective photothermal agents which meet the basic requirements of excellent absorption, superior photothermal conversion capacity as well as satisfactory light stability when exposed to a laser. Traditional thermal contrast biosensors make use of heat produced by enzymatic reactions to detect concentrations of analyte, which exist drawbacks of time-consumption and the need of expensive instrumentation [29–31]. So far, lots of photothermal sensors with thermal-imager or thermometers as novel signal modes have been explored to overcome these weaknesses above. For example, Yu et al. used a thermal imager as thermal response signal output to detect cTnI protein based on $Cu_{2-x}Ag_xS$ NPs [32]. Bu et al. used a thermometer as signal output system to monitor biothiols based on the formation of PDA NPs [33].

Nanozymes, as one kind of burgeoning nanomaterials possessing enzyme-mimicking activity, have attracted a wide range of interest in many areas since the first discovery of unique peroxidase-like activity in Fe_3O_4 NPs [34,35]. Nanozymes can overcome many common drawbacks existing in natural enzymes, such as high cost, difficulties in purification, poor stability, *etc.* [36,37] So far, various nanozymes have been created and applied to catalyze enzymatic reactions, such as metal oxide nanozymes, metal-organic frameworks, carbon-based nanozymes, metal sulfides and so on [38–42]. Metal-nitrogen-doped carbon (M-N-C), carbon incorporated with nitrogen and metallic element, has emerged as one of the most promising nanozymes, which is attributed to the M-Nx sites parallel to natural metal enzymes [43,44]. In recent decades, various synthesis strategies of M-N-C have been created and a big step forward has been got in exploring the active sites and electrochemical application of M-N-C. Researchers gained ideal structures of M-N-C by choosing appropriate isolated metal sites, regulating the coordination environment to regulate products of the CO_2 reduction reaction. Compared with electrocatalysis, there is only a small amount of tasks for constructing versatile sensing platforms based on M-N-C nanozymes [45,46].

Herein, a photothermal and colorimetric biosensor was established to realize the accurate and flexible detection of AChE and its inhibitors (Paraoxon-ethyl, a model of OPs) (Scheme 1). First, we successfully synthesized Fe–N–C with remarkable peroxidase-mimetic activity by hydrothermal synthesis method under the existence of formamide (FA) [47]. As a nanozyme with splendid peroxidase-mimetic activity, Fe–N–C was employed as the catalyst of H_2O_2 to further accelerate the oxidation of 3,3′,5,5′-tetramethylbenzidine (TMB) with a color change. Oxidation TMB showed outstanding photothermal conversion capacity under the irradiation of 808 nm laser that could convert analyte concentration information into a visible thermal signal. Therefore, we could receive the temperature signal in 1.0 min from a near-infrared imaging camera. This study provides a simple detection method for AChE and its inhibitors to realize point-of-care testing. Such detection methods can further be expanded to monitor other molecules relevant to the production or consumption of H_2O_2.

2. Experimental

2.1. Preparation of Fe–N–C or CN

Fe–N–C was synthesized by the hydrothermal method according to the previous report with minor modification. First, $FeN_3O_9{\cdot}9H_2O$ (242 mg) was put into formamide (60 mL) and stirred for 5 min. Then the mixture was diverted into 100 mL Teflon-lined autoclave and heated at a constant temperature of 180 °C for 12 h. The product was then centrifuged and washed thoroughly three times. At last, the sediment was put into a vacuum oven to obtain pure Fe–N–C. The CN was synthesized similarly in the absence of iron nitrate nonahydrate.

2.2. Peroxidase activity of Fe–N–C

TMB was utilized as chromogenic reagents to confirm the peroxidase-like activity of Fe–N–C. Firstly, deionized water (538 μL), acetate buffer (200 μL, 200 mM, pH 4.2), TMB (100 μL, 10 mM), H_2O_2 (150 μL, 20 mM) and Fe–N–C (12 μL, 0.1 mg mL^{-1}) were adequately mixed. The mixed solution was placed at room temperature for 20 min to incubate. Eventually, the absorbance values (652 nm) were obtained. The absorbance values (652 nm) of Fe–N–C/TMB/H_2O_2 system with different concentrations of H_2O_2 (0–1.0 mM) or TMB (0–0.30 mM) were measured.

The kinetic data were calculated through Michaelis-Menten equation:

$$v = \frac{\mathrm{Vmax}\ [\mathrm{S}]}{\mathrm{Km}\ + [\mathrm{S}]}$$

In above equation, v symbolizes the initial rate of enzymatic reaction, V_{max} symbolizes maximum reaction velocity, [S] symbolizes the concentration of substrate, and K_m symbolizes the Michaelis-Menten constant.

2.3. Colorimetric and photothermal sensing of AChE activity

AChE standard solution (50 μL) with different concentrations, phosphate buffer (50 μL, 200 mM, pH 7.4) and ATCh (20 μL, 10 mM) were mixed in the mixture and further diluted to 360 μL and incubated at 37 °C for 5 min. Then, Fe–N–C (12 μL, 0.1 mg mL^{-1}) was input and incubated for 2 min. After incubating for 2 min, acetate buffer (200 μL, 200 mM, pH 4.2), TMB (100 μL, 10 mM), H_2O_2 (150 μL, 20 mM) and deionized water (178 μL) were added and reacted for 20 min. After these procedures, colorimetric and photothermal detection could be performed. The absorption spectra measurement was carried out at room temperature. And the temperature was monitored by near-infrared imaging camera when the reaction system was irradiated by 808 nm laser (1.5 W cm^{-2}) for 1.0 min.

2.4. Colorimetric and photothermal sensing of paraoxon-ethyl

At first, AChE (100 μL, 400 mU/mL) and paraoxon-ethyl (50 μL) were mixed and incubated for 5 min. Subsequently, phosphate buffer (50 μL, 200 mM, pH 7.4), ATCh (20 μL, 10 mM) and deionized water (140 μL) were added into the above solution to incubate at 37 °C for 5 min. Next procedures were same to colorimetric and photothermal detection of AChE activity.

3. Results and discussions

3.1. Synthesis and characterization of Fe–N–C

The Fe–N–C nanozymes were synthesized *via* hydrothermal treatment at 180 °C for 12 h by using formamide as raw material. Besides, CN was successfully synthesized with the same procedure as a control. Firstly, the morphology of Fe–N–C and CN were characterized by transmission electron microscopy (TEM). TEM shows that the CN consists of stacked and irregular sheets (Fig. 1A). The morphology of Fe–N–C (Fig. 1D) remains similar to CN except for the bigger size after introducing Fe. Similar to CN (Fig. 1B), the high-resolution TEM (HRTEM) image (Fig. 1E) uncovers that Fe–N–C exhibits layer structure and the absence of metal nanoparticles/nanoclusters, demonstrating the metal nanoparticles/nanoclusters-free Fe–N–C. Compared to CN (Fig. S1 and Fig. 1C), elemental mapping images (Fig. 1F) and corresponding EDX spectrum (Fig. S2) of Fe–N–C show uniform distribution of Fe (0.96%), N (3.51%) and C (95.53%), demonstrating that Fe inserts in CN. The aberration-corrected HAADF-STEM image of Fe–N–C (Fig. S3) demonstrates the well-dispersed Fe single atom species on the Fe–N–C. There are many bright spots with atomic-scale belong to Fe atoms and not any nanoparticles/nanoclusters in Fe–N–C.

Additionally, the X-ray diffraction (XRD) pattern of Fe–N–C displays a distinct peak at about 27° distributed to (002) plane of the carbon nitride phase (Fig. S4). Further, the surface elemental state of Fe–N–C was verified by X-ray photoelectron spectroscopy (XPS). The valence states of C (1s) and N (1s) and Fe (2p) elements closely associated with Fe–N–C can obviously be observed in full XPS survey spectrum (Fig. 2A). The N 1s spectrum was separated into double asymmetric peaks situated at 398.5 eV and 400.1 eV, which belong to pyridinic and pyrrolic (Fig. 2B). As expected, two forms of N species are propitious to the combination with iron ions. In the meantime, the high-resolution spectrum of Fe 2p displays a double peak with binding energies of 708.79 and 721.59 eV, which can be attributed to characteristic spin-orbit split Fe $2p_{3/2}$ and Fe $2p_{1/2}$ of divalent iron, respectively (Fig. 2C). The double asymmetric peaks of Fe 2p XPS spectra indicate that Fe species are oxidation states rather than metallic states in Fe–N–C [47]. The result further demonstrates there are no metal nanoparticles in Fe–N–C.

3.2. Peroxidase-mimetic activity of Fe–N–C

To demonstrate the peroxidase-mimetic activity of Fe–N–C, comparative experiments were carried out. As shown in Fig. 3A, the absorbance of control groups including the TMB solution (curve a), the mixture of TMB and H_2O_2 (curve b), the Fe–N–C solution (curve c) and the mixture of TMB and Fe–N–C (curve d) appear lower. Only the mixture containing TMB, Fe–N–C and H_2O_2 displays a distinct color of blue and a significant absorption at 652 nm (curve e). The experiments certify that neither Fe–N–C or H_2O_2 can be lack in the oxidation of TMB, indicating that Fe–N–C possesses remarkable peroxidase-like activity. Furthermore, electron paramagnetic resonance (EPR) was employed to study Fe–N–C solution with or without H_2O_2. As is evident from Fig. 3B, no free radicals or vacancies can be observed without H_2O_2. However, four peaks with a standard height ratio (1:2:2:1) corresponding to •OH were obtained in EPR spectrum. Based on the above experiments, the conclusion that Fe–N–C possesses strong peroxidase-mimetic activity and generates •OH to oxidize TMB by H_2O_2 can be drawn.

For the purpose of obtaining the catalytic ability of Fe–N–C, the steady-state kinetics experiment of the Fe–N–C/H_2O_2/TMB system was systematically implemented by keeping the condition constant except the TMB or H_2O_2 concentrations. The concentration of TMB or H_2O_2 and

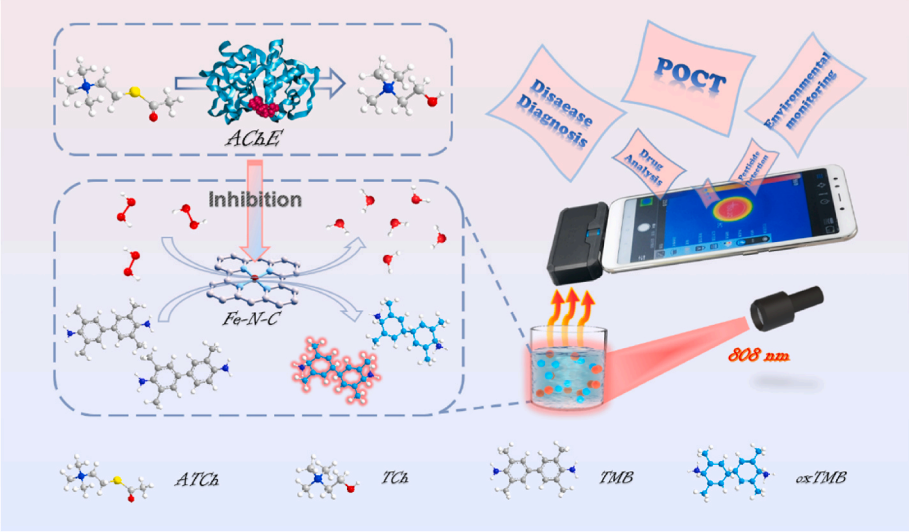

Scheme 1. Schematic illustration of photothermal and colorimetric detection of AChE based on Fe–N–C nanozymes.

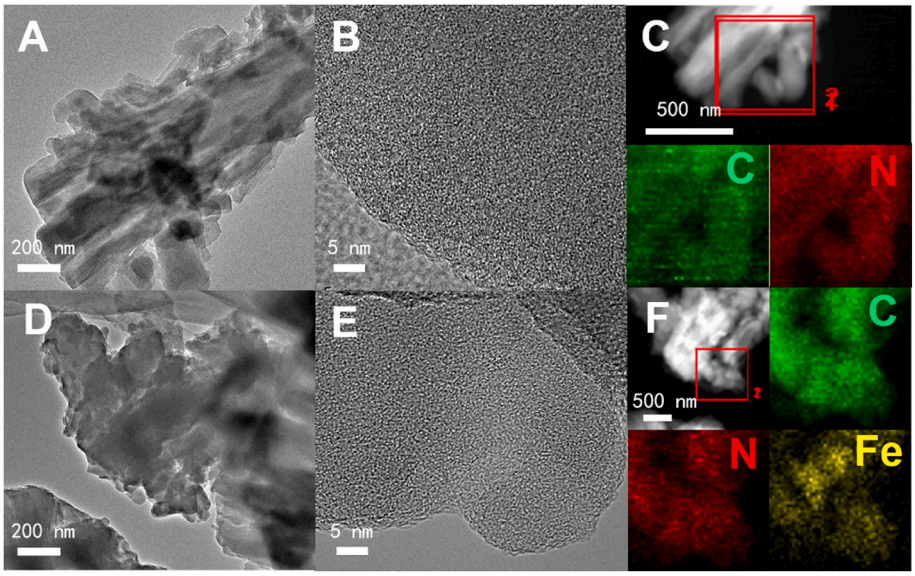

Fig. 1. TEM images and HRTEM images of CN (A, B) and Fe–N–C (D, E); (C, F) HAADF-STEM and elemental mapping images of CN (C and N) and Fe–N–C(C, N and Fe).

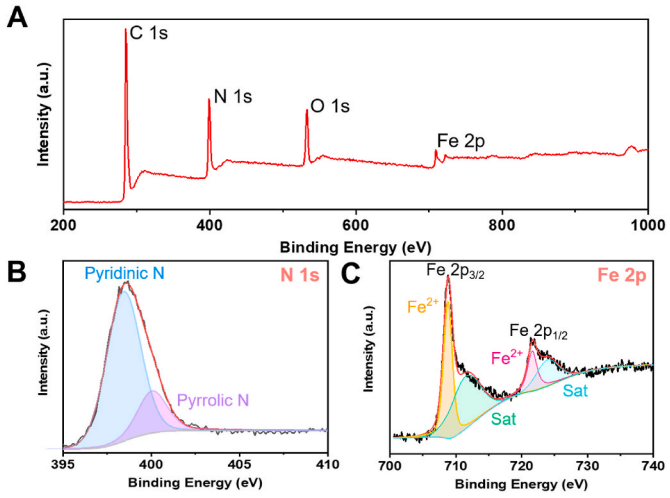

Fig. 2. (A) XPS survey spectra of Fe–N–C; high-resolution XPS spectra of (B) N 1s; and (C) Fe 2p.

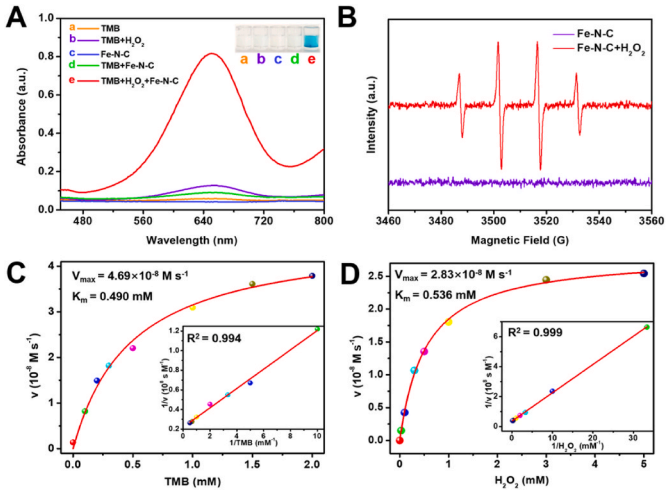

Fig. 3. (A) UV–vis absorption spectra of TMB with different contents (insets are the corresponding solutions with different colors; (B) EPR spectrum of Fe–N–C with (red line) and without (purple line) H_2O_2; Michaelis-Menten kinetics and relevant double reciprocal plots for Fe–N–C nanozyme with (C) TMB and (D) H_2O_2 as the substrates (inset: plotting double reciprocal). (For interpretation of the references to color in this figure legend, the reader is referred to the Web version of this article.)

the associated initial reaction rate and the relationship between them can be obtained (the experiment was performed under the same condition in Fig. S5 and Fig. S6, similarly hereinafter). It can be obviously discovered both TMB and H_2O_2 are fitted with the Michaelis-Menten model well (Fig. 3C–D). The significant steady-state kinetics parameters (K_m, V_{max}) are got from the slopes and intercepts of the Lineweaver-Burk double reciprocal plot (Fig. 3C–D, inset). K_m is a representative indicator of enzyme affinity to homologous substrates. The lower K_m value implies that the enzyme is more capable of binding to a substrate. The K_m and V_{max} of horseradish peroxidase (HRP) and some reported peroxidase mimics are summarized in Table S1. It can be confirmed that K_m values of Fe–N–C with both TMB and H_2O_2 are equal to HRP as well as other artificial enzymes, demonstrating that Fe–N–C possesses superior binding ability with TMB and H_2O_2.

3.3. Feasibility investigation of AChE detection

The binding of sulfhydryl molecules to Fe–N–C leads to a decrease in the peroxidase-mimetic activity of Fe–N–C, as reported from previous work [48]. In consideration of the ability of AChE to promote the mercapto molecules production, we design to construct a sensor based on Fe–N–C to monitor AChE. Fe–N–C in the Fe–N–C/H_2O_2/TMB/ATCh/-AChE system (AChE detection system) can act as a catalyst to encourage the generation of •OH by H_2O_2. However, AChE can catalyze the decomposition of ATCh to generate thiocholine (TCh). Then, TCh, a sort of mercapto molecule, possesses the ability to block the binding sites of Fe–N–C to inhibit peroxidase-mimetic activity. We speculate that the readout signal of the AChE detection system decreases with increasing AChE concentration.

To further test the feasibility of the AChE detection system, the absorbance and temperature difference (irradiation by 808 nm laser for 1.0 min) of control groups (Fig. 4A and Fig. 4B) were recorded. The addition of AChE has a certain negative effect on the decrease of the absorbance and temperature difference of Fe–N–C. Moreover, it is can be

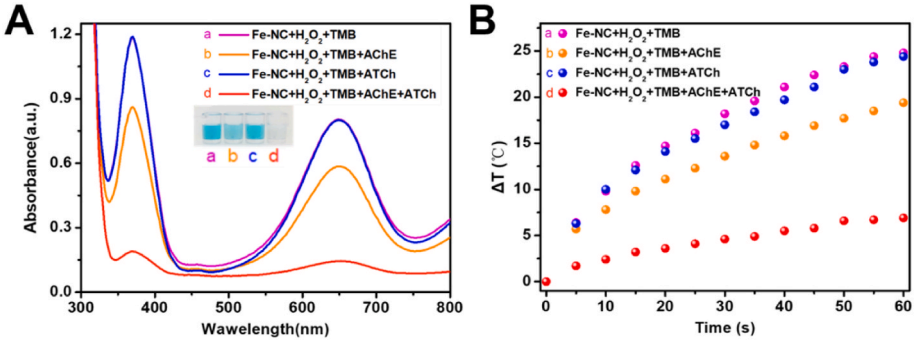

Fig. 4. (A) UV–vis spectra (insets are the corresponding solutions with different colors) and (B) temperature increment by 808 nm irradiation at 1.5 W cm^{-2} of solutions contain: (a) Fe–N–C + TMB + H_2O_2, (b) Fe–N–C + TMB + H_2O_2 + AChE, (c) Fe–N–C + TMB + H_2O_2 + ATCh, and (d) Fe–N–C + TMB + H_2O_2 + AChE + ATCh. (For interpretation of the references to color in this figure legend, the reader is referred to the Web version of this article.)

found that ATCh nearly has any impact on Fe–N–C/H_2O_2/TMB system. As expected, the absorbance and temperature difference decreases significantly when AChE and ATCh coexist in the system and the solution is nearly colorless. Based on the above results, it is demonstrated that the colorimetric and photothermal strategy for the AChE detection by this system is feasible.

3.4. Dual-mode colorimetric and photothermal detection of AChE

Under the optimal conditions, the strategy was carried out to detect various concentrations of AChE through the colorimetric signal and thermal signal readout. The reaction system exhibits a color variation from colorless to blue when the concentration of AChE increases from 0 to 40 mU mL^{-1} (Fig. 5A, inset). At the same time, the absorbance enhances proportionally as the AChE level increases (Fig. 5A). Moreover, a good linearity could be established between the absorbance (652 nm) and the logarithm of the AChE level within the dynamic range from 3 to 40 mU mL^{-1} (Fig. 5B). The linear regression equation is $\Delta A_{652\ nm} = 0.453 \times \lg C_{AChE} - 0.11$ (mU mL^{-1}, $R^2 = 0.997$) with a limit of detection

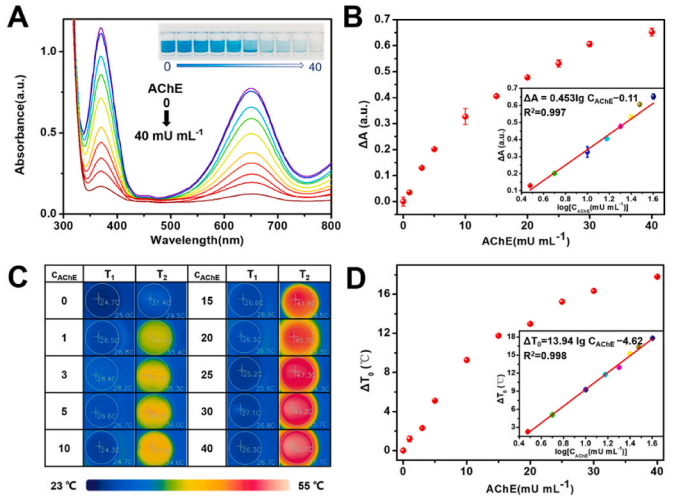

Fig. 5. (A) UV–vis spectra of AChE detection system with AChE concentration from 0 to 40 mU mL^{-1} (insets are corresponding solutions with different colors). (B) The absorbance (652 nm) of different activities of AChE detection system ($\Delta A = A_0 - A$, A_0 is the absorbance without AChE, inset is the linearity between AChE activity and absorbance values). (C) photograms of AChE detection system with different AChE activity (0–40 mU mL^{-1}) before and after irradiation. (D) The temperature increment of different activities of AChE detection system ($\Delta T_0 = T_1$ - T, T_0 is the temperature increment without AChE, inset is the linearity between AChE activity and temperature increments). (For interpretation of the references to color in this figure legend, the reader is referred to the Web version of this article.)

(LOD) of 1.9 mU mL^{-1} (S/N = 3). Although qualitative or semi-quantitative information can be obtained from the color readout detected by the naked eye, a UV–vis absorption spectrometer is still in need for accurately quantifying the AChE concentration in some real samples.

To meet diversified detection demand for AChE, such as in site testing, the AChE detection system was further developed to realize the quantitative sensing performance by using a near-infrared imaging camera as a reader (Fig. S7). The temperatures of reaction systems with various amounts of AChE were recorded during the irradiation of 808 nm laser for 1.0 min. From a near-infrared imaging camera, we can not only observe the colors related to different temperatures but also obtain the accurate temperatures displayed on smartphone (Fig. 5C). As illustrated in Fig. 5D, it can be found that the temperature increments and the AChE concentrations ranging from 3 to 40 mU mL^{-1} have a good linear correlation. The linear regression equation is expressed as $\Delta T_0 = 13.94 \times \lg C_{AChE} - 4.62$ (mU mL^{-1}, $\Delta T_0 = T_2 - T_1$, where T_2 and T_1 are the temperature measurements of the reaction system with and without irradiation), and LOD is 2.2 mU mL^{-1} (S/N = 3). This result demonstrates that it is potential for our strategy applied in establishing a portable photothermal detection platform for AChE activity and the LOD of our sensor is equal to former reports (Table S1).

To further demonstrate the potential application of the dual-mode colorimetric and photothermal strategy, the AChE activity analysis was performed by testing human serum samples. Table S3 reveals that the recoveries vary from 96.23% to 101.0% (colorimetric) and from 98.00% to 102.4% (photothermal) and the relative standard deviation (RSD) was all satisfactory (<3.9%). Accordingly, it can be indicated that the sensor constructed can be employed to monitor AChE in human serum. For the purpose of proving the reusability of Fe–N–C, we tried to reclaim Fe–N–C which has be used to reacting with H_2O_2. As illustrated in Fig. S8, the absorbance and temperature were able to maintain 93.74% and 92.66% signal intensities after washing, indicating that Fe–N–C has acceptable catalytic stability.

3.5. Specificity of the colorimetric and photothermal platform

Specificity is also a crucial evaluation index for a sensing platform. Therefore, the specificity of the AChE detection system was studied by measuring a series of common interfering materials (GOx, UA, GLu, Kana, K^+, Na^+ and Mg^{2+}) using both the colorimetric and photothermal assays (Fig. 6A and Fig. 6B). There is little apparent absorbance and temperature changes can be observed for the interfering materials compared to the blank value, while temperature increment and absorbance decreases can be obviously observed in the presence of target AChE. The conclusion can be drawn that the constructed sensing platform possesses satisfactory anti-interference ability. Similarly, to verify that the sensor possesses good specificity in actual sample detection, the anti-interference experiments in human serum and river water were

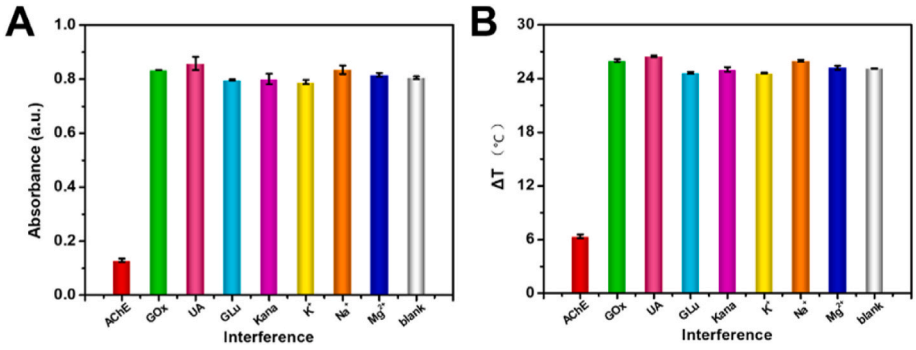

Fig. 6. The selectivity of AChE detection strategy by (A) UV–vis and (B) NIR imaging camera detection.

carried out. The experimental results (Fig. S9 and Fig. S10) show that the system is potential for AChE detection with specificity in human serum and river water.

3.6. Dual-mode colorimetric and photothermal detection of inhibitor of AChE (paraoxon-ethyl)

Although Ops, as one kind of pesticide, is widely applied in modern agriculture and has brought great economic benefits, unfortunately, the residue of Ops causes a series of questions (ecosystem destruction, food contamination, etc.) [49,50]. It is urgent to develop an accurate and facile method for Ops contamination in food monitor for protecting human health. So far lots of sensors have emerged for the detection of Ops. Among these sensors, the sensor based on AChE (the primary target of Ops) is the most widely used sensor for OPs trace. To develop the application of AChE detection system, it was expanded to monitor Ops concentration (one of the AChE inhibitions) due to its inhibition of AChE activity.

Paraoxon-ethyl was selected to be a model of Ops for the study of AChE inhibitions detection due to its negligible influence on Fe–N–C/TMB/H_2O_2 system (Fig. S11). As expected, the activity of AChE can be inhibited when AChE is incubated with paraoxon-ethyl (Fig. 7A). Both colorimetric and photothermal signals can be found to have a regular change with the increase of paraoxon-ethyl concentration. As seen in Fig. 7B, the absorbance of oxTMB at a peak of 652 nm increases with the paraoxon-ethyl addition increases. There is a good linearity could be established between the absorbance (652 nm) and the logarithm of paraoxon-ethyl concentration in the scope of 0.03–2 μg mL^{-1} (Fig. 7C). The linear regression equation can be noted as $\Delta A_{652\ nm} = 0.123 \times \lg C_{AChE} + 0.402$ (μg mL^{-1}, $R^2 = 0.984$) with a LOD of 0.012 μg mL^{-1} (S/N = 3). As seen in Fig. 7D, the increment of temperature also linearly decreases with the logarithm of paraoxon-ethyl concentration in the range of 0.03–2 μg mL^{-1}. The linear regression equation is $\Delta T = 3.07 \times \lg C_{AChE} + 12.97$ (μg mL^{-1}, $\Delta T = T_2 - T_1$, where T_2 and T_1 are the temperature measurements of the reaction system before and after laser irradiation) with a limit of detection of 0.013 μg mL^{-1} (S/N = 3).

We also tested the recoveries of paraoxon-ethyl in environmental samples (tap water and river water) to verify the possibility of the Fe–N–C-based dual-mode biosensor for practical applications (Table S4). The recoveries ranging from 96.23% to 102% in the colorimetric method and 96.6% to 104.2% in the photothermal method, respectively, demonstrate that the biosensor possesses promising potential in analyzing real samples with outstanding accuracy.

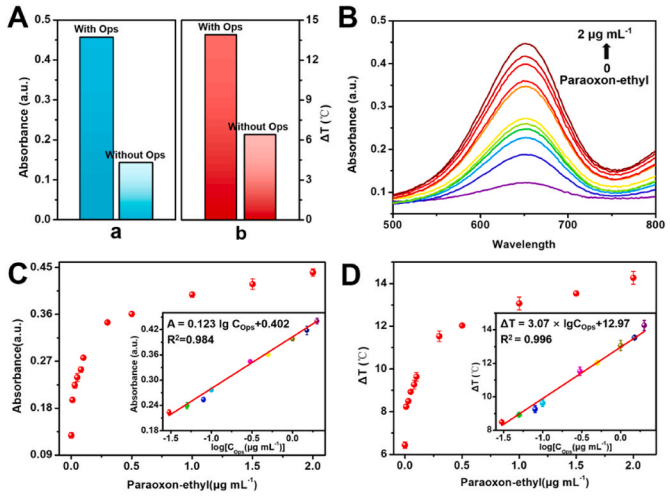

Fig. 7. (A) UV–vis spectra (a) and (b) temperature increment by 808 nm irradiation at 1.5 W cm^{-2} of system paraoxon-ethyl detection with and without Ops (paraoxon-ethyl); (B) UV–vis spectra of paraoxon-ethyl detection system with the concentrations of paraoxon-ethyl from 0 to 2 μg mL^{-1}; (C) The absorbance at 652 nm of different activities of paraoxon-ethyl detection system (inset is the corresponding linearity between paraoxon-ethyl concentration and variations of absorbance values); (D) The temperature increment of different activities of paraoxon-ethyl detection system ($\Delta T = T_1 - T_2$, T_2 and T_1 are the temperature measurements of the reaction system before and after laser irradiation, inset is the linearity between paraoxon-ethyl concentration and variations of temperature increments).

4. Conclusions

In summary, a dual-mode colorimetric and photothermal biosensor based on the Fe–N–C-mediated TMB-H_2O_2 system was successfully designed for the simple, cost-effective detection of AChE. Fe–N–C with remarkable peroxidase-mimetic is employed to catalyze the oxidation of TMB acting as both colorimetric and photothermal reagent. Compared to other reported instrumental methods, the photothermal platform based on the readout of a portable near-infrared imaging camera shows excellent advantages for low-cost and portable detection in resource-poor settings. Moreover, the dual-mode analytical assay integrating colorimetric and photothermal signals both display excellent stability can realize mutual authentication, providing more convincing results. The satisfactory recovery rates of AChE activity in human serum and Ops in tap water and river water demonstrate the method possesses good practicability. Thus, the proposed sensor provides a promising platform for reliable detection of AChE and its inhibitors in real samples.

CRediT authorship contribution statement

Liling Lu: Conceptualization, Methodology, Writing – original draft. **Xuehan Hu:** Visualization, Data curation, Writing – review & editing. **Ruijin Zeng:** Visualization, Investigation, Writing – review & editing. **Qianyun Lin:** Visualization, Investigation, Writing – original draft. **Xue Huang:** Visualization, Data curation, Data Collection, Writing – original draft. **Meijin Li:** Visualization, Data curation, Data Collection, Writing – original draft. **Dianping Tang:** Methodology, Visualization,

Supervision, Funding acquisition, Project administration.

Declaration of competing interest

The authors declare that they have no known competing financial interests or personal relationships that could have appeared to influence the work reported in this paper.

Data availability

Data will be made available on request.

Acknowledgments

The authors acknowledge financial support from the National Natural Science Foundation of China (grant nos.: 21874022 & 21675029).

Appendix A. Supplementary data

Supplementary data to this article can be found online at https://doi.org/10.1016/j.aca.2022.340383.

References

[1] D. Liu, B. Xu, C. Dong, Recent advances in colorimetric strategies for acetylcholinesterase assay and their applications, Trends Anal. Chem. 142 (2021), 116320.
[2] R. Jin, Z. Xing, D. Kong, X. Yan, F. Liu, Y. Gao, P. Sun, X. Liang, G. Lu, Sensitive colorimetric sensor for point-of-care detection of acetylcholinesterase using cobalt oxyhydroxide nanoflakes, J. Mater. Chem. B 7 (2019) 1230–1237.
[3] X. Yan, Y. Song, X. Wu, C. Zhu, X. Su, D. Du, Y. Lin, Oxidase-mimicking activity of ultrathin MnO_2 nanosheets in colorimetric assay of acetylcholinesterase activity, Nanoscale 9 (2017) 2317–2323.
[4] T. Han, G. Wang, Peroxidase-like activity of acetylcholine-based colorimetric detection of acetylcholinesterase activity and an organophosphorus inhibitor, J. Mater. Chem. B 7 (2019) 2613–2618.
[5] N. Inestrosa, A. Alvarez, C. Perez, R. Moreno, M. Vicente, C. Linker, O. Casanueva, C. Soto, J. Garrido, Acetylcholinesterase accelerates assembly of amyloid-beta-peptides into Alzheimer's fibrils: possible role of the peripheral site of the enzyme, Neuron 16 (1996) 881–891.
[6] T. Fedorova, L. Seidelin, K. Knudsen, A. Schacht, J. Geday, N. Pavese, D. Brooks, P. Borghammer, Decreased intestinal acetylcholinesterase in early Parkinson disease, Neurology 88 (2017) 775–781.
[7] M. Campanari, M. Garcia-Ayllon, S. Ciura, J. Saez-Valero, E. Kabashi, Neuromuscular junction ipairment in ayotrophic lteral slerosis: rassessing the role of aetylcholinesterase, Front. Mol. Neurosci. 9 (2016) 160.
[8] R. Zeng, Z. Luo, L. Zhang, D. Tang, Platinum nanozyme-catalyzed gas generation for pressure-based bioassay using polyaniline nanowires-functionalized graphene oxide framework, Anal. Chem. 90 (2018) 12299–12306.
[9] R. Zeng, Z. Luo, L. Su, L. Zhang, D. Tang, R. Niessner, D. Knopp, Palindromic molecular beacon based Z-scheme BiOCl-Au-CdS photoelectrochemical biodetection, Anal. Chem. 91 (2019) 2447–2454.
[10] B. Jiang, L. Meng, N. Zou, H. Wang, S. Li, L. Huang, X. Cheng, Z. Wang, W. Chen, C. Wang, Mechanism-based pharmacokinetics-pharmacodynamics studies of harmine and harmaline on neurotransmitters regulatory effects in healthy rats: challenge on monoamine oxidase and acetylcholinesterase inhibition, Phytomedicine 62 (2019), 152967.
[11] H. Wang, J. Wang, C. Timchalk, Y. Lin, Magnetic electrochemical imunoassays with quantum dot lables detection of posphorylated acetylcholinesterase in plasma, Anal. Chem. 80 (2008) 8477–8484.
[12] X. Hu, C. Dinu, Nanoporous gold electrode for ultrasensitive detection of neurotoxin fasciculin, Anal. Chem. 1085 (2019) 91–97.
[13] L. Yu, J. Chang, X. Zhuang, H. Li, T. Hou, F. Li, Two-dimensional cobalt-doped Ti_3C_2 MXene nanozyme-mediatedhomogeneous electrochemical strategy for pesticides assay based on in situ generation of electroactive substances, Anal. Chem. 94 (2022) 3669–3676.
[14] N. Morato, D. Holden, R. Cooks, High-throughput label-free enzymatic assays using desorption electrospray-ionization mass spectrometry, Angew. Chem. Int. Ed. 59 (2020) 20459–20464.
[15] F. Ma, C. Yuan, J. Liu, J. Cao, D. Wu, Colorimetric immunosensor based on Au@g-C_3N_4-doped spongelike 3D network cellulose hydrogels for detecting alpha-fetoprotein, ACS Appl. Mater. Interfaces 11 (2019) 19902–19912.
[16] Y. Choi, J. Hwang, S. Lee, Recent trends in nanomaterials-based colorimetric detection of pathogenic bacteria and viruses, Small Methods 2 (2018), 1700351.
[17] R. Zeng, J. Wang, Q. Wang, D. Tang, Y. Lin, Horseradish peroxidase-encapsulated DNA nanoflowers: an innovative signal-generation tag for colorimetric biosensor, Talanta 221 (2021), 121600.
[18] X. Li, L. Yang, C. Men, Y. Xie, J. Liu, H. Zou, Y. Li, L. Zhan, C. Huang, Photothermal soft nanoballs developed by loading plasmonic Cu_2-xSe nanocrystals into liposomes for photothermal immunoassay of Aflatoxin B-1, Anal. Chem. 91 (2019) 4444–4450.
[19] R. Zeng, Y. Tang, L. Zhang, Z. Luo, D. Tang, Dual-readout aptasensing of antibiotic residues based on gold nanocluster-functionalized MnO_2 nanosheets with target-induced etching reaction, J. Mater. Chem. B 6 (2018) 8071–8077.
[20] C. Lin, Y. Zhu, J. Yu, X. Qin, X. Xian, F. Tsow, E. Forzani, D. Wang, N. Tao, Gradient-based colorimetric sensors for continuous gas monitoring, Anal. Chem. 90 (2018) 5375–5380.
[21] R. Ren, G. Cai, Z. Yu, D. Tang, Glucose-loaded liposomes for amplified colorimetric immunoassay of streptomycin based on enzyme-induced iron(II) chelation reaction with phenanthroline, Sensor. Actuator. B Chem. 265 (2018) 174–181.
[22] Z. Gao, Z. Qiu, M. Lu, J. Shu, D. Tang, Hybridization chain reaction-based colorimetric aptasensor of adenosine 5 '-triphosphate on unmodified gold nanoparticles and two label-free hairpin probes, Biosens. Bioelectron. 89 (2017) 1006–1012.
[23] X. Zheng, Q. Lian, L. Zhou, Y. Jiang, J. Gao, Peroxidase mimicking of binary polyacrylonitrile-CuO nanoflowers and the application in colorimetric detection of H_2O_2 and ascorbic acid, ACS Sustain. Chem. Eng. 9 (2021) 7030–7043.
[24] L. Xin, H. Lei, White peroxidase-mimicking nanozymes: white peroxidase-mimicking nanozymes: colorimetric pesticide assay without interferences of O_2 and color, Adv. Funct. Mater. 30 (2020), 2070184-2070184.
[25] Y. Xiong, L. Su, F. Ye, S. Zhao, Ultrasmall phosphatase-mimicking nanoceria with slight self-colour for nonredox nanozyme-based colorimetric sensing, Anal. Chim. Acta 1200 (2022), 339604.
[26] G. Cai, Z. Yu, P. Tong, D. Tang, Ti_3C_2 MXene quantum dot-encapsulated liposomes for photothermal immunoassays using a portable near-infrared imaging camera on a smartphone, Nanoscale 11 (2019) 15659–15667.
[27] G. Fu, S. Sanjay, W. Zhou, R. Brekken, R. Kirken, X. Li, Exploration of nanoparticle-mediated photothermal effect of TMB-H_2O_2 colorimetric system and its application in a visual quantitative photothermal immunoassay, Anal. Chem. 90 (2018) 5930–5937.
[28] L. Huang, J. Chen, Z. Yu, D. Tang, Self-powered temperature sensor with seebeck effect transduction for photothermal-thermoelectric coupled immunoassay, Anal. Chem. 92 (2020) 2809–2814.
[29] M. Yakovleva, S. Bhand, B. Danielsson, The enzyme thermistor-A realistic biosensor concept: a critical review, Anal. Chim. Acta 766 (2013) 1–12.
[30] S. Xu, X. Bai, L. Wang, Exploration of photothermal sensors based on photothermally responsive materials: a brief review, Inorg. Chem. Front. 5 (2018) 751–759.
[31] R. Zeng, H. Gong, Y. Li, Y. Li, W. Lin, D. Tang, D. Knopp, CRISPR-Cas12a-derived photoelectrochemical biosensor for point-of-care diagnosis of nucleic acid, Anal. Chem. 94 (2022) 7442–7448.
[32] Z. Yu, H. Gong, J. Xu, Y. Li, F. Xue, Y. Zeng, X. Liu, D. Tang, Liposome-embedded $Cu_{2-x}Ag_xS$ nanoparticle-mediated photothermal immunoassay for daily monitoring of cTnI protein using a portable thermal imager, Anal. Chem. 94 (2022) 7408–7416.
[33] T. Bu, Y. Tian, J. Ma, M. Zhang, F. Bai, S. Zhao, K. He, X. Sun, Y. Wang, L. Wang, Polydopamine-mediated photothermal effect enables a new method for point-of-care testing of biothiols using a portable photothermal sensor, Sensor. Actuator. B Chem. 346 (2021), 130498.
[34] L. Gao, J. Zhuang, L. Nie, J. Zhang, Y. Zhang, N. Gu, T. Wang, J. Feng, D. Yang, S. Perrett, X. Yan, Intrinsic peroxidase-like activity of ferromagnetic nanoparticles, Nat. Nanotechnol. 2 (2007) 577–583.
[35] M. Liang, X. Yan, Nanozymes: from new concepts, mechanisms, and standards to applications, Acc. Chem. Res. 52 (2019) 2190–2200.
[36] W. Duan, Z. Qiu, S. Cao, Q. Guo, J. Huang, J. Xing, X. Lu, J. Zeng, Pd-Fe_3O_4 Janus nanozyme with rational design for ultrasensitive colorimetric detection of biothiols, Biosens. Bioelectron. 196 (2022), 113724.
[37] X. Zhou, M. Wang, J. Chen, X. Xie, X. Su, Peroxidase-like activity of Fe-N-C single-atom nanozyme based colorimetric detection of galactose, Anal. Chim. Acta 1128 (2020) 72–79.
[38] X. Zhang, S. Lin, S. Liu, X. Tan, Y. Dai, F. Xia, Advances in organometallic/organic nanozymes and their applications, Coord. Chem. Rev. 429 (2021), 213652.
[39] H. Sun, Y. Zhou, J. Ren, X. Qu, Carbon nanozymes: enzymatic properties, catalytic mechanism, and applications, Angew. Chem. Int. Ed. 57 (2018) 9224–9237.
[40] R. Zeng, K. Lian, B. Su, L. Lu, J. Lin, D. Tang, S. Lin, X. Wang, Versatile synthesis of hollow metal sulfides via reverse cation exchange reactions for photocatalytic CO_2 reduction, Angew. Chem. Int. Ed. 60 (2021) 25055–25062.
[41] K. Tripathi, H. Ahn, M. Chung, X. Le, D. Saini, A. Bhati, S. Sonkar, M. Kim, T. Kim, N, S, and P-Co-doped carbon quantum dots: intrinsic peroxidase activity in a wide pH range and its antibacterial applications, ACS Biomater. Sci. Eng. 6 (2020) 5527–5537.
[42] P. Nguyen, J. Lee, A. Cho, M. Kim, D. Choi, J. Han, M. Kim, J. Lee, Rational development of Co-doped mesoporous ceria with high peroxidase-mimicking activity at neutral pH for paper-based colorimetric detection of multiple biomarkers, Adv. Funct. Mater. 32 (2022), 2112428.
[43] B. Yan, F. Wang, S. He, W. Liu, C. Zhang, C. Chen, Y. Lu, Peroxidase-like activity of Ru-N-C nanozymes in colorimetric assay of acetylcholinesterase activity, Anal. Chim. Acta 1191 (2022), 339362.
[44] M. Kim, J. Lee, H. Kim, A. Cho, K. Shim, T. Le, S. An, J. Han, M. Kim, J. Lee, Heme cofactor-resembling Fe–N single site embedded graphene as nanozymes to selectively detect H_2O_2 with high sensitivity, Adv. Funct. Mater. 30 (2020), 1905410.
[45] H. Xu, D. Wang, P. Yang, A. Liu, R. Li, Y. Li, L. Xiao, X. Ren, J. Zhang, M. An, Atomically dispersed M-N-C catalysts for the oxygen reduction reaction, J. Mater. Chem. A 8 (2020) 23187–23201.

[46] C. Zhao, B. Li, J. Liu, Q. Zhang, Intrinsic electrocatalytic activity regulation of M-N-C single-atom catalysts for the oxygen reduction reaction, Angew. Chem. Int. Ed. 60 (2021) 4448–4463.
[47] C. Zhang, C. Chen, D. Zhao, G. Kang, F. Liu, F. Yang, Y. Lu, J. Sun, Multienzyme cascades based on highly efficient metal-nitrogen- carbon nanozymes for construction of versatile bioassays, Anal. Chem. 94 (2022) 3485–3493.
[48] Y. Wu, L. Jiao, X. Luo, W. Xu, X. Wei, H. Wang, H. Yan, W. Gu, B. Xu, D. Du, Y. Lin, C. Zhu, Oxidase-like Fe-N-C single-atom nanozymes for the detection of acetylcholinesterase activity, Small 15 (2019), 1903108.
[49] J. Chang, H. Li, T. Hou, F. Li, Paper-based fluorescent sensor for rapid naked-eye detection of acetylcholinesterase activity and organophosphorus pesticides with high sensitivity and selectivity, Biosens. Bioelectron. 86 (2016) 971–977.
[50] R. Ma, M. Xu, C. Liu, G. Shi, J. Deng, T. Zhou, Stimulus response of GQD-sensitized Tb/GMP ICP nanoparticles with dual-responsive ratiometric fluorescence: toward point-of-use analysis of acetylcholinesterase and organophosphorus pesticide poisoning with acetylcholinesterase as a biomarker, ACS Appl. Mater. Interfaces 12 (2020) 42119–42128.